Supplementary information

Experimental Section

Materials and Methods

Materials

2-methoxyethanol (MOE, 99.8%, Aladdin), AgCl (99.5%, Innochem), CuCl (99.999%, Alfa), $Zn(CH_3COO)_2$ (99.99%, Aladdin), $SnCl_4$ (99.998%, Macklin), thiourea (99.99%, Aladdin) were sourced from the specified suppliers, and Se pellets (99.999%, Zhong Nuo Advanced Material) were purchased accordingly. Notably, thiourea was recrystallized twice prior to use.

Film Preparation

A precursor solution was prepared by dissolving thiourea (2.92 g), CuCl (0.87 g), AgCl (0.14 g), $Zn(CH_3COO)_2$ (1.18 g), and $SnCl_4$ (1.59 g) in 11 mL of 2-methoxyethanol (MOE) with continuous stirring. After filtration, the solution was spin-coated onto precleaned Mo substrates at 3000 rpm for 30 seconds. The coated substrates were then annealed on a hot plate at 280 °C for 2 minutes. This process was repeated to form a CZTS precursor film approximately 1.5 μm thick. The precursor films were selenized in a rapid thermal processing (RTP) furnace by placing them in a graphite box containing Se pellets. The temperature was ramped to 550 °C over 1 min, held for 16 min, then cooled to room temperature.

Device Preparation

ZTO films were fabricated using the Fiji-G2 system (Nanotech), $[Zn(C_2H_5)_2]$ as the Zn precursor, $[Sn(N(CH_3)_2)_4]$ as the Sn precursor, and H_2O as the oxygen source. A 15-nm thick ZTO buffer layer was deposited, with four different Zn:Sn ratios (3:1, 4:1, 5:1, and 6:1). To create a high-quality CZTSSe/ZTO heterojunction, JHT was performed in ventilated air conditions with humidity between 40% and 70%, at different temperatures for 7 minutes, followed by natural cooling. Since JHT-processed heterojunction thin films (CZTSSe/ZTO) are sensitive to long-term storage, a 330 nm ITO layer was sputtered at 100 W under a mixed Ar/O_2 atmosphere at 0.35 Pa. A 100-

nm Ag electrode and a 110-nm MgF_2 layer were deposited by thermal evaporation. The highest-performing solar cell achieved a certified efficiency of 13.90% on a 0.0481 cm^2 aperture, as verified by the South China National Center of Metrology (SCM).

Film Characterizations

XRD measurements were performed using a Rigaku Ultima IV diffractometer. Raman spectra were collected using a Renishaw in Via Raman spectrometer with a 532 nm excitation laser. KPFM data were obtained with a Bruker Multimode system, while UPS was conducted using a PHI 5000 Versa Probe. TEM lamellae were prepared with a FIB system. Cross-sectional TEM imaging and elemental distribution analysis were performed using a double Cs-corrected TEM (Titan Cubed Themis G2300) with EDX. XPS measurements were carried out with a PHI 5000 VersaProbe III.

Device Characterizations

The J–V characteristics were measured under AM 1.5G illumination (100 mW/cm^2) at 25 °C using a Keithley 2400 SourceMeter. Small-area devices had an aperture area of 0.0481 cm^2, while large-area devices covered approximately 1.03 cm^2. The performance of the champion device was certified by the South China National Metrology Centre (SCM). EQE spectra were obtained with a Zolix solar cell characterization system. C–V and DLCP measurements were performed using a Keithley 4200A-SCS parameter analyzer and a JANIS cryogenic probe station. TRPL was measured with a TimeHarp 260 system using time-correlated single-photon counting (TCSPC). J–V–T measurements were carried out with a Lakeshore 325 temperature controller and a Keithley 4200A-SCS system. EIS was conducted using a CHI660E electrochemical workstation. AS measurements were performed with a Victor Digital LCR meter across a temperature range of 300–170 K. M-TPC/M-TPV measurements were performed with a dedicated setup, and EBIC measurements were performed using a TESCAN VEGA 3HBS system.

Supplementary Figures

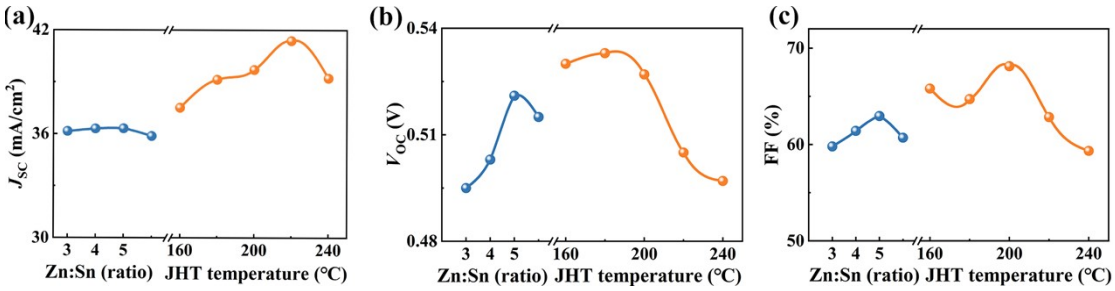

Fig. S1. Device parameter trends. Combined effect of Zn:Sn ratio and JHT temperature on CZTSSe device performance.

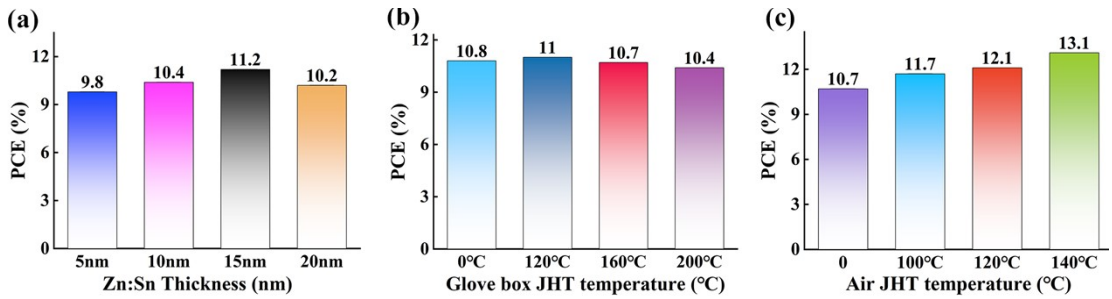

Fig. S2. Key factors influencing the efficiency of CZTSSe solar cells. (a) Dependence of device performance on the thickness of the ZTO buffer layer, (b) Impact of glove-box-based JHT on device efficiency, (c) Efficiency trends under air-ambient low-temperature JHT, showing a positive correlation with temperature.

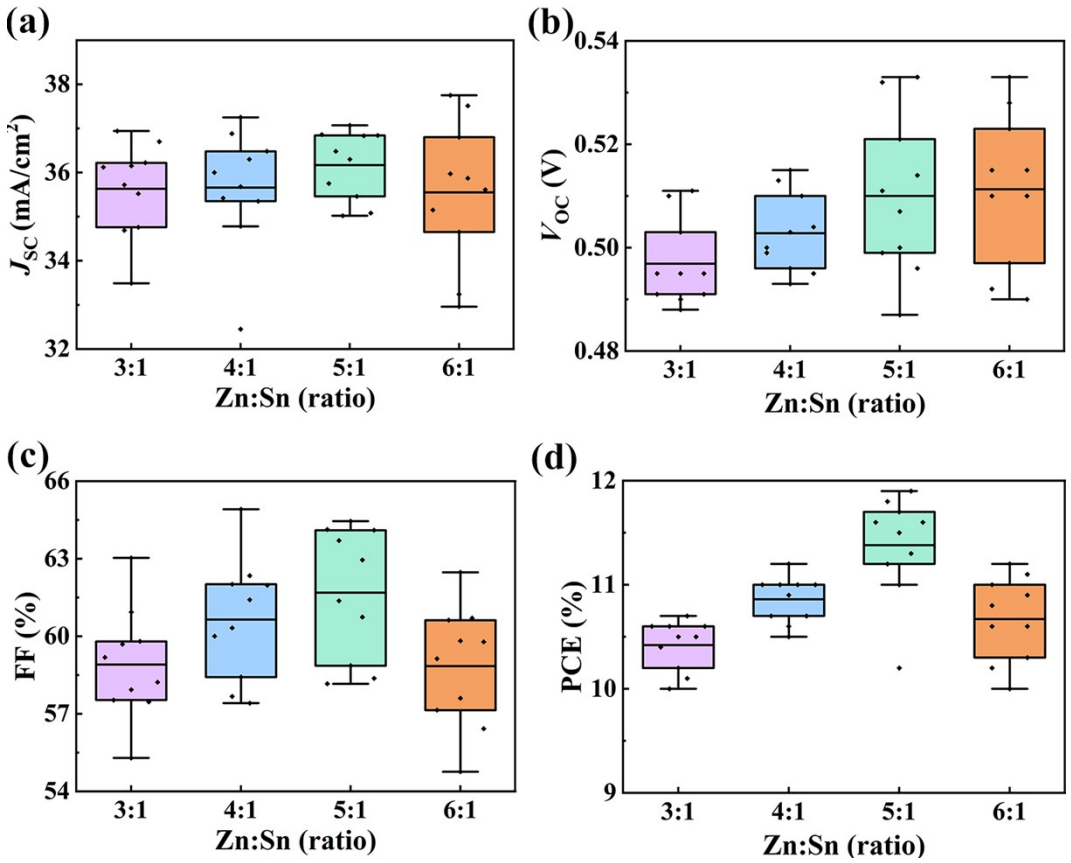

Fig. S3. Effect of the Zn:Sn ratio on photovoltaic performance. n = 10 devices were measured for each Zn:Sn ratio: (a) J_{SC}, (b) V_{OC}, (c) FF, and (d) PCE.

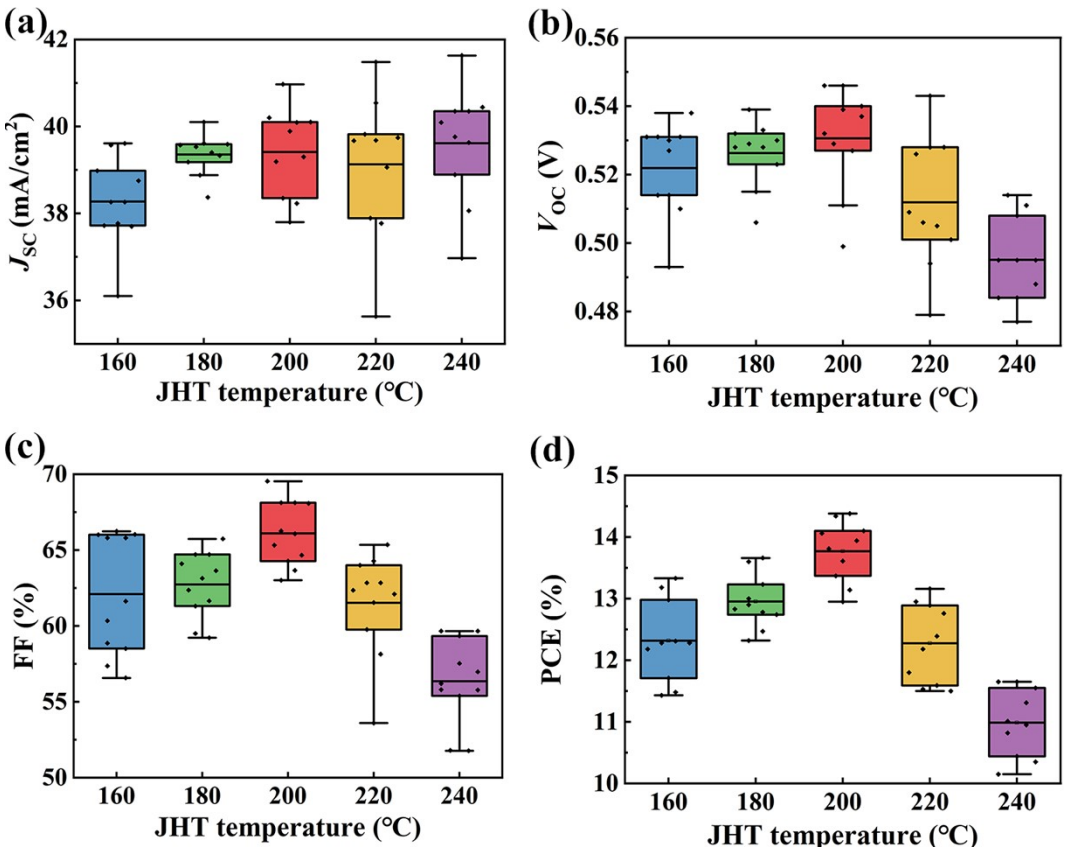

Fig. S4. Impact of ventilated-air JHT temperature on photovoltaic parameters of CZTSSe/ZTO devices: (a) J_{SC}, (b) V_{OC}, (c) FF, and (d) PCE. For each temperature, n = 10 devices were measured; for the 200 °C condition, devices were obtained from two independent fabrication batches. The PCE statistics (mean ± SD) are: 160 °C, 12.32% ± 0.67%; 180 °C, 12.95% ± 0.44%; 200 °C, 13.77% ± 0.49%; 220 °C, 12.28% ± 0.64%; and 240 °C, 10.99% ± 0.55%.

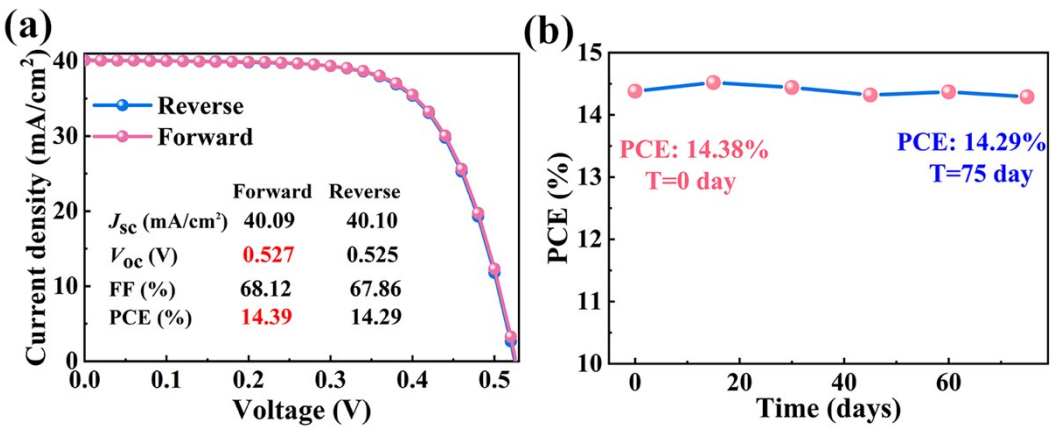

Fig. S5. (a) J–V characteristics of JHT-200 devices measured under both forward and reverse scan directions, (b) Evolution of PCE for the champion device stored in ambient conditions without encapsulation for a period of 75 days.

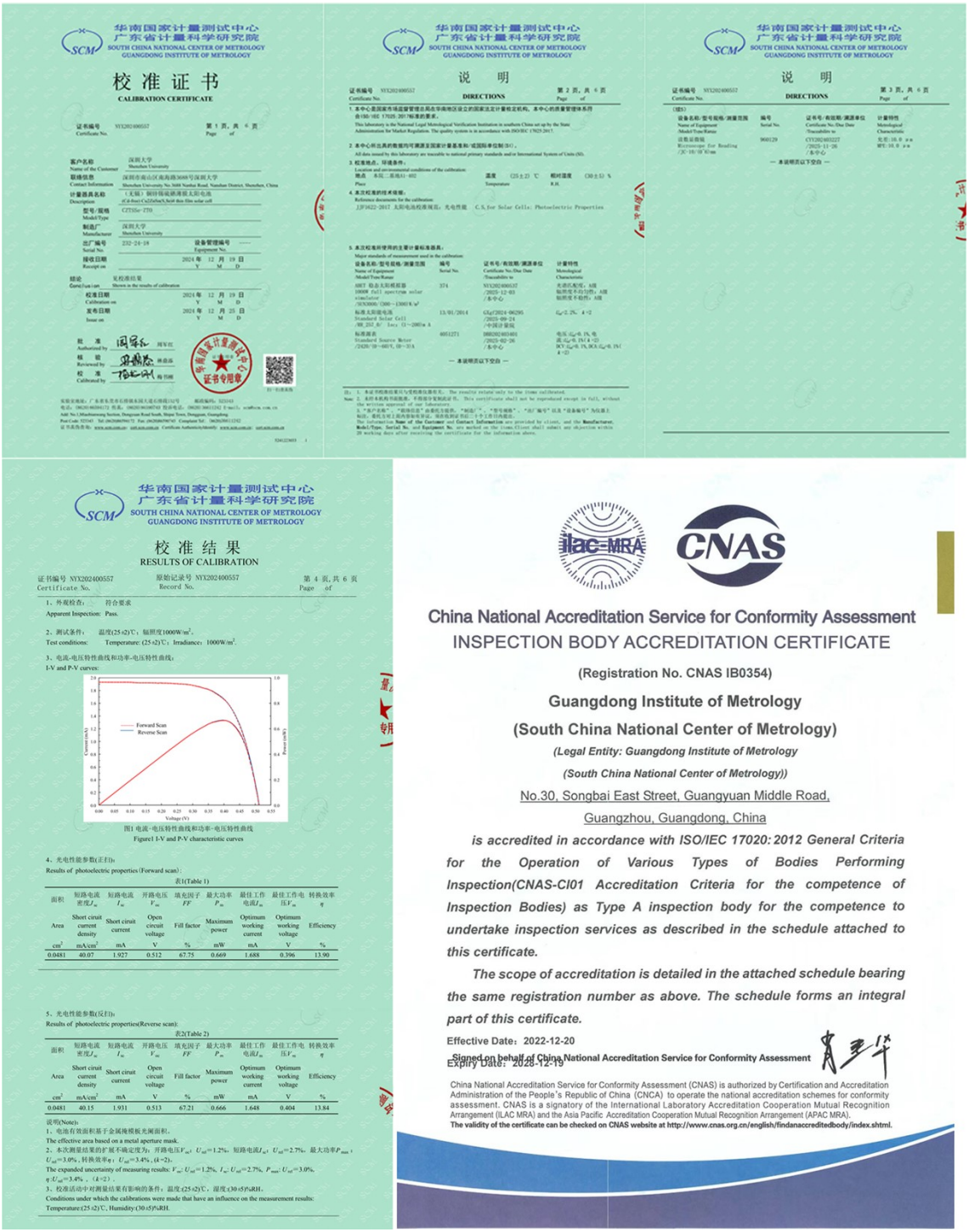

Fig. S6. Certified efficiency report. Certified power conversion efficiency (PCE) of 13.90% measured by the South China National Center of Metrology (SCM) under standard test conditions (AM 1.5G, 100 mW/cm^2, 25°C).

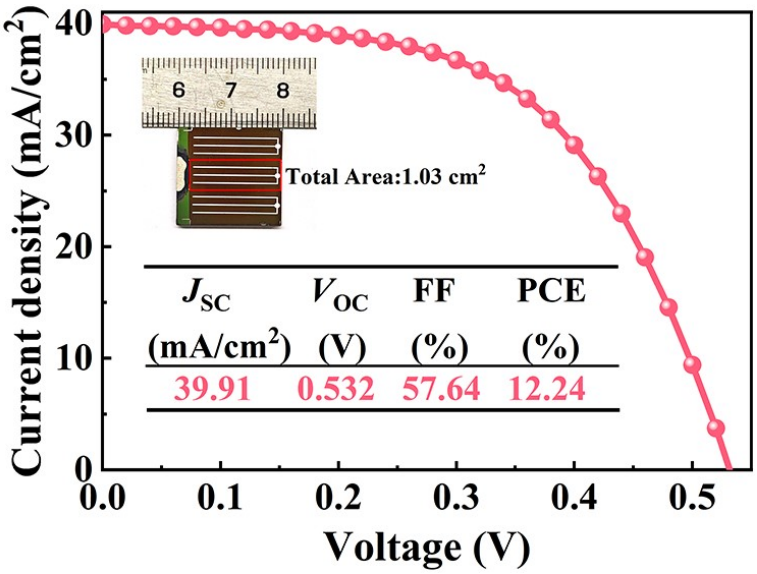

Fig. S7. The J–V curve of the large-area Cd-free CZTSSe solar cell.

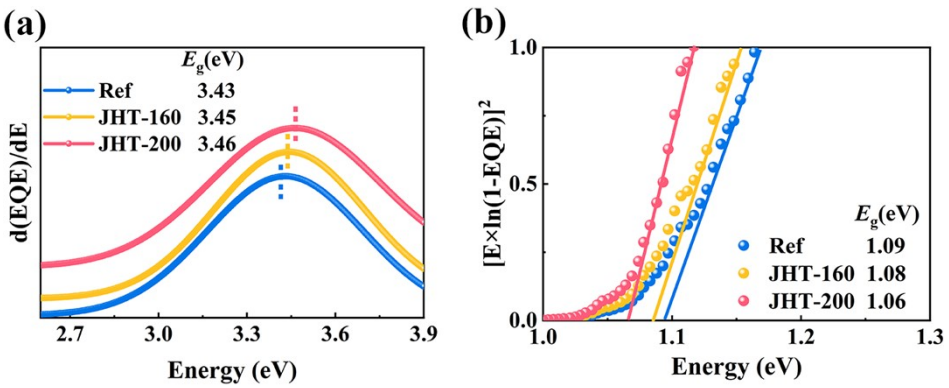

Fig. S8. Performance characterization and bandgap analysis of CZTSSe solar cells. (a) Bandgap determination of the ZTO layer through derivative analysis of the external quantum efficiency (d(EQE)/dE vs. photon energy). (b) CZTSSe absorber bandgap extraction from EQE spectral response.

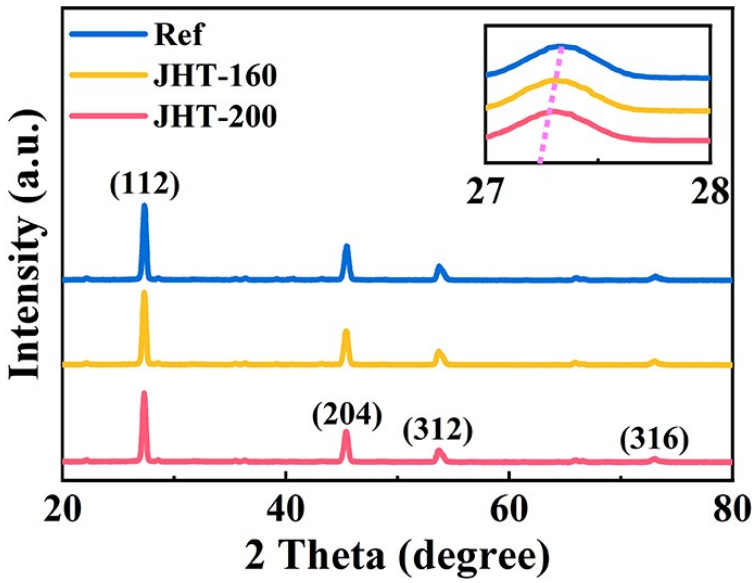

Fig. S9. XRD patterns of films. Comparison of the crystallographic structures between the Ref and JHT-200 samples based on their X-ray diffraction (XRD) patterns.

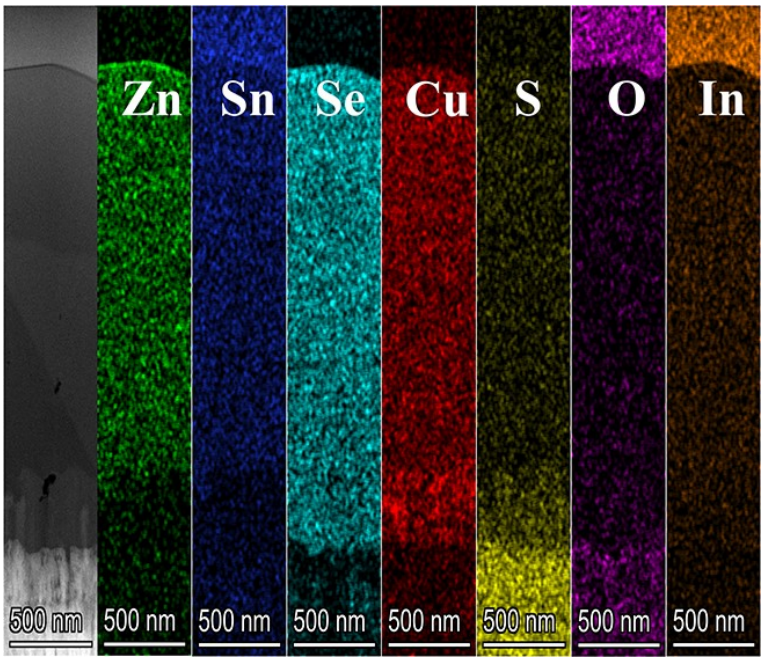

Fig. S10. Cross-sectional energy-dispersive X-ray spectroscopy (EDX) elemental mapping of Cu, Zn, Sn, Se, O and In distributions.

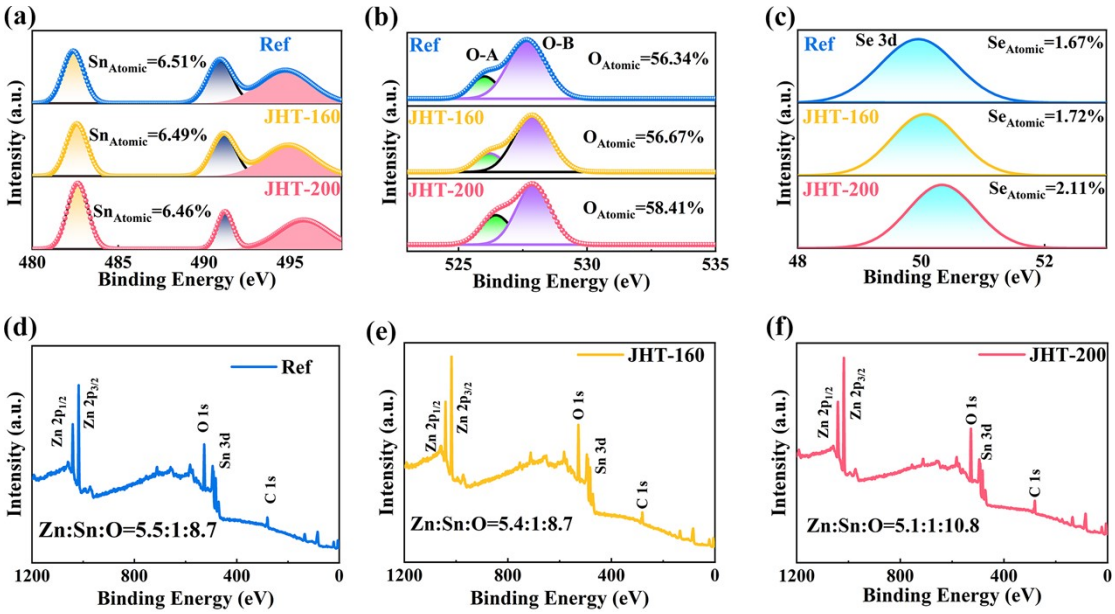

Fig. S11. X-ray photoelectron spectroscopy analysis of CZTSSe/ZTO films. XPS spectra showing (a) Sn 3d, (b) O 1s, and (c) Se 3d. Full-range XPS spectra comparing (d) Ref, (e) JHT-160, and (f) JHT-200 samples.

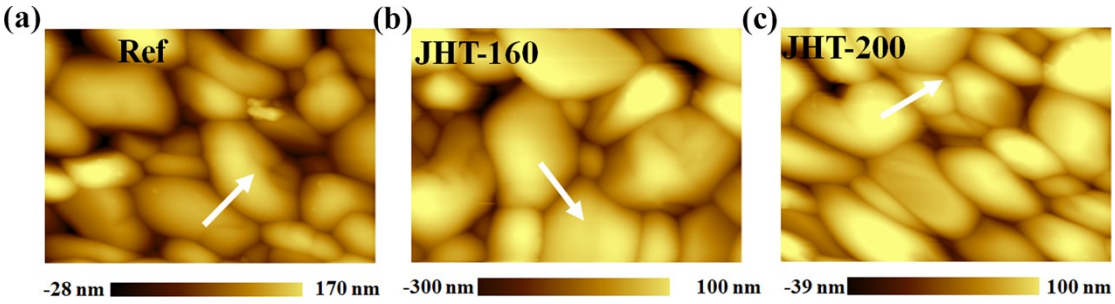

Fig. S12. Kelvin probe force microscopy (KPFM) images of (a) Ref/ZTO, (b) JHT-160/ZTO, and (c) JHT-200/ZTO samples showing topographic contrast.

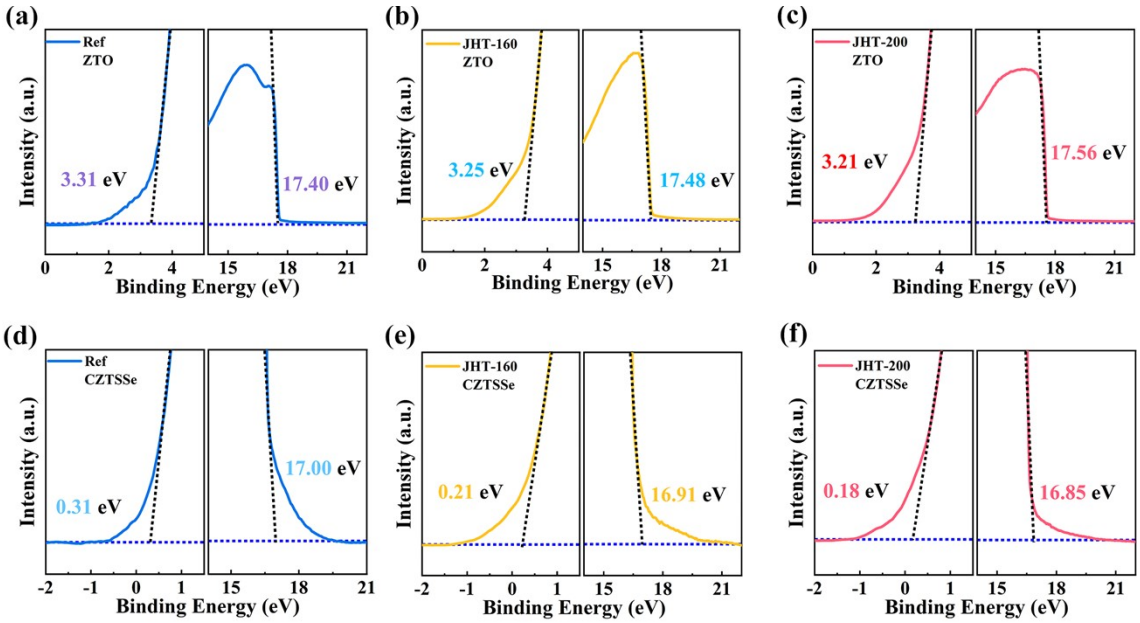

Fig. S13. Electronic structure characterization of CZTSSe and ZTO films. Valence band spectra and secondary electron cut-off edges were used to determine the Fermi level position relative to the valence band maximum.

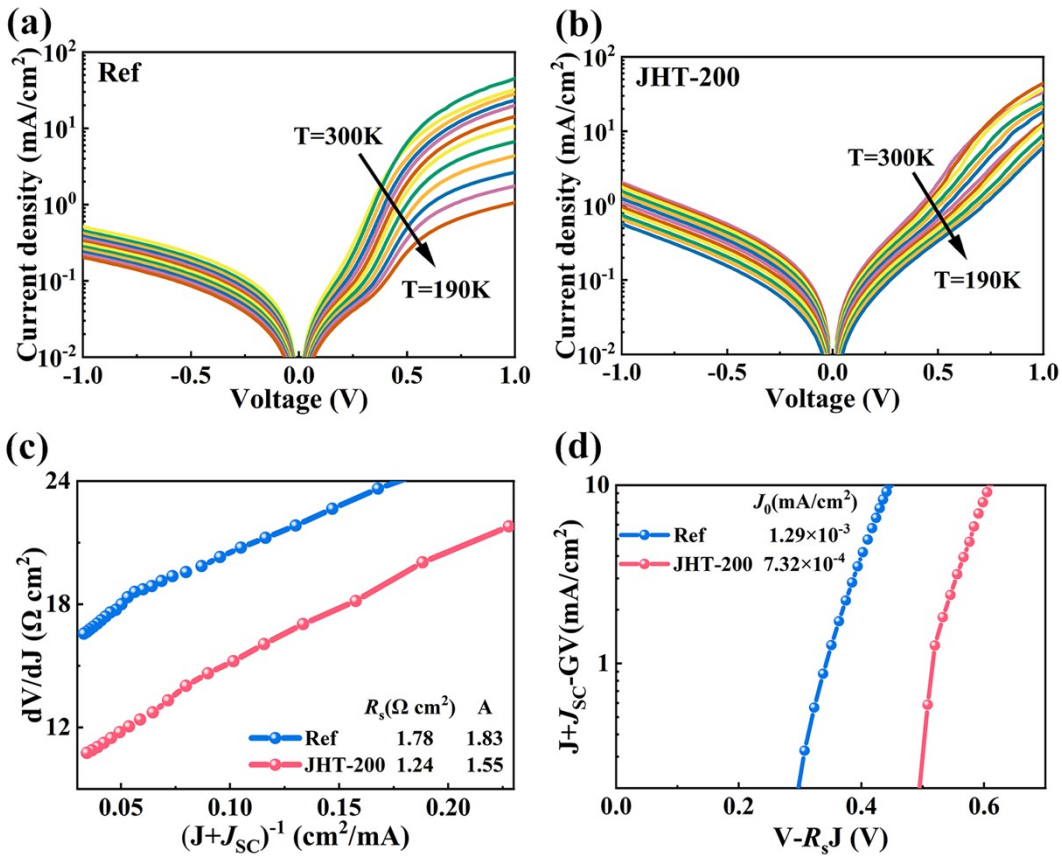

Fig. S14. Temperature-dependent dark J–V characteristics. (a) Ref, (b) JHT-200. (c) Extracted series resistance (Rs) and ideality factor (A), (d) Extracted reverse saturation current density (J_0).

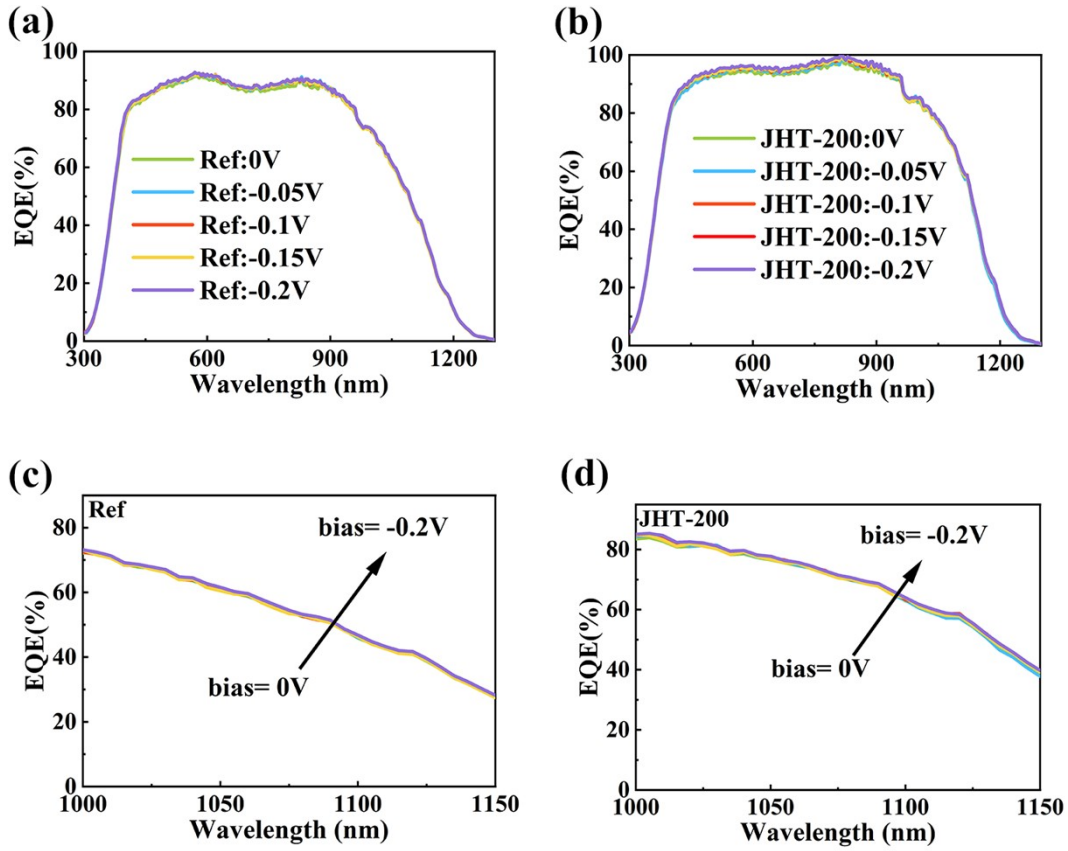

Fig. S15. EQE spectra of CZTSSe devices with bias ranging from 0 to -0.2V. (a, c) Ref and (b, d) JHT-200 devices.

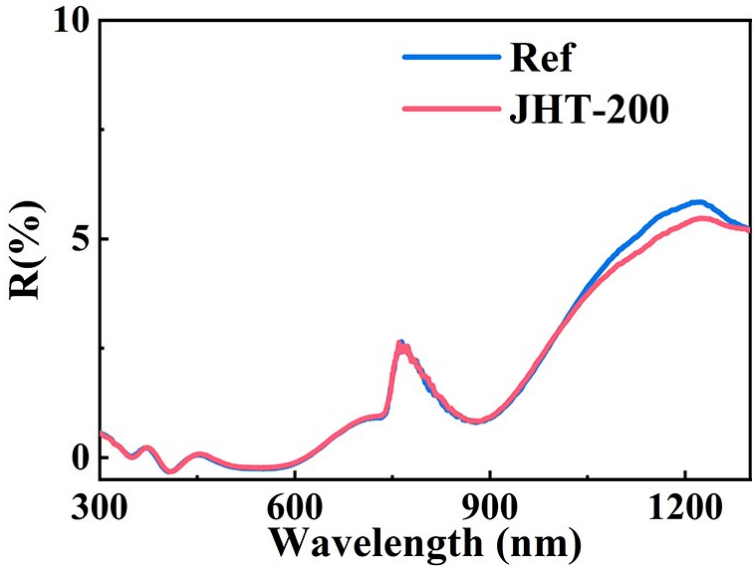

Fig. S16. The reflection data measured using ultraviolet-visible (UV-Vis) spectroscopy.

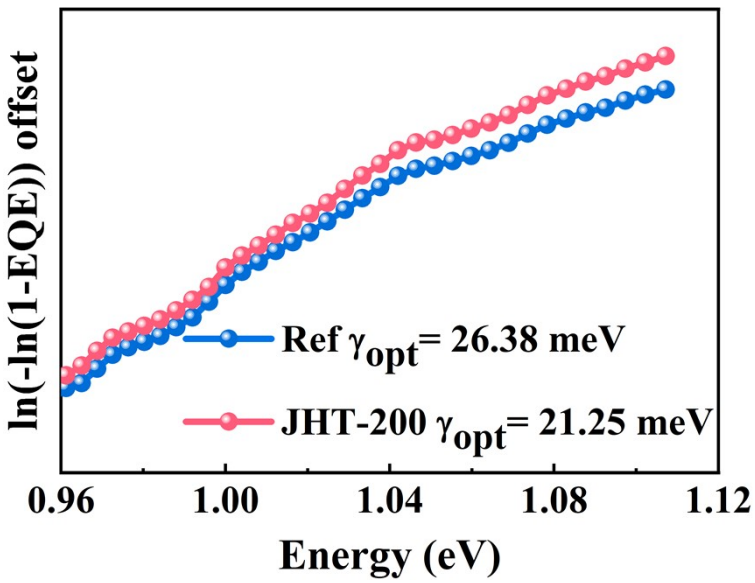

Fig. S17. Fluctuations in electrostatic potential derived from EQE fitting results.

Supplementary Tables

Table S1. Detailed parameters of Ref, JHT-160, and JHT-200 devices.

J_{SC}(mA/cm^2)	V_{OC}(V)	FF(%)	PCE(%)	E_g(eV)	$V_{oc,def}$(V)	E_u(meV)	CBO(eV)
36.30	0.521	62.95	11.91	1.09	0.328	32.41	-0.26
38.26	0.530	65.80	13.34	1.08	0.310	29.10	-0.10
40.09	0.527	68.12	14.39	1.06	0.294	26.41	0.08

Table S2. Summary of device parameters and performance ratios J_{SC}/J_{SC}^{SQ} and V_{OC}/V_{OC}^{SQ} for reported CZTSSe solar cells.

Buffer layer	J_{SC}(mA/cm^2)	V_{OC}(V)	FF(%)	PCE(%)	E_g(eV)	J_{SC}/J_{SC}^{SQ}(%)	V_{OC}/V_{OC}^{SQ}(%)	Reference
Spin-Coated-PCBM	29.40	0.370	49.1	5.33	1.02	62.4	47.2	NENU[1]
CBD-ZnS(O,OH)	32.60	0.332	51.8	5.60	1.00	67.6	43.4	IREC[2]
CBD-ZnS(O,OH)	29.00	0.389	52.0	5.80	1.06	64.2	47.4	CEA[3]
ALD-ZTO	34.10	0.414	60.8	8.60	1.08	76.5	49.3	NTU[4]
Sputtered-ZTO	36.50	0.401	59.6	8.70	1.08	81.9	47.7	FZU[5]
Sputtered-ZTO	35.91	0.426	58.6	8.95	1.06	79.4	51.9	JLU[6]
ALD-Zn(O,S)	35.60	0.496	56.0	9.82	1.09	80.3	58.4	CNU[7]
ALD-SnO_2	34.36	0.462	64.0	10.10	1.11	77.9	53.2	CNU[8]
Sputtered-ZTO	36.39	0.445	69.3	11.22	1.07	81.2	53.6	INU[9]
ALD-ZTO	36.28	0.498	66.5	11.80	1.08	81.4	59.3	SZU[10]
CBD-CdS	40.60	0.423	67.3	11.60	1.00	84.2	55.3	IBM[11]
CBD-CdS	37.00	0.555	71.5	14.90	1.08	83.0	65.8	CAS[12]
ALD-ZTO (This work)	40.09	0.527	68.1	14.39	1.06	88.7	64.2	This work

Supplementary Notes

Note S1. UPS analysis

The electronic band structure characteristics of the ZTO thin films, including the conduction band minimum (E_C), valence band maximum (E_V), and Fermi level (E_F), were determined from the experimentally obtained secondary electron cutoff (Ecutoff) and valence band (V_B) spectra using the following theoretical framework. In this framework, ϕ represents the work function of the sample, hv is the photon energy, and *E*g is the bandgap of the sample, as calculated from the external quantum efficiency (EQE). E_{vacuum} denotes the vacuum level (0 eV), and χ is the electron affinity of the sample[13]:

$$\varphi = hv - E_{cutoff}$$

$$E_V = \phi + VB$$

$$E_C = E_V - E_g$$

$$\chi = E_{vacuum} - E_C$$

Note S2. CV and DLCP analysis

Capacitance-voltage (CV) and drive-level capacitance profiling (DLCP) techniques are commonly used to characterize carrier concentration and depletion width in thin-film solar cells. The fundamental equations used for these analyses are as follows[14]:

$$N_{CV} = \frac{C^3}{qA^2\varepsilon_0\varepsilon}\left(\frac{dC}{dV}\right)^{-1}$$

$$W_{d-CV} = \frac{\varepsilon_0\varepsilon A}{C}$$

$$N_{DL} = -\frac{C_0^3}{2q\varepsilon_0\varepsilon A^2 C_1}$$

$$W_{d-DL} = \frac{\varepsilon_0\varepsilon A^2}{C_0}$$

$$N_{IT} = N_{CV} - N_{DLCP}$$

where q is the elementary charge, A is the solar-cell area, ε_0 is the vacuum permittivity, ε is the relative dielectric constant of CZTSSe, and C_0 and C_1 are two parameters obtained from the quadratic fit.

Note S3. TRPL analysis

The minority carrier lifetime is determined by fitting the TRPL curve to a bi-exponential function[15]:

$$y = y_0 + A_1 e^{-\frac{x}{t_1}} + A_2 e^{-\frac{x}{t_2}}$$

$$\tau_{avg} = \frac{A_1\tau_1^2 + A_2\tau_2^2}{A_1\tau_1 + A_2\tau_2}$$

where τ_1 and τ_2 are the lifetimes, and A_1 and A_2 are the corresponding amplitude ratios (relative weights) of the τ_1 and τ_2 components.

Note S4. J-V-T analysis

$$A ln J_0 = A ln J_{00} - (\frac{E_a}{kT})$$

A represents the ideal factor, J_0 is the reverse saturation current density, and J_{00} is the prefactor dependent on the recombination path. E_a, k, and T denote the recombination activation energy, Boltzmann constant, and temperature, respectively. From the equation, E_a can be determined by plotting ln J_0 against 1/kT and examining the slope[16].

Note S5. AS analysis

Admittance spectral measurements are used to estimate the defect levels within the bandgap. The inflection frequency ω_0 of each admittance spectrum is determined by the corner frequency at the maximum point of the $-\omega(dC/d\omega)$ plot, which is fitted using the following equation[17]:

$$\omega_0 = 2\pi v_0 T^2 e^{-\frac{E_a}{KT}}$$

$$E(\omega) = KT\, ln\left(\frac{2\pi v_0 T^2}{\omega}\right)$$

$$N_t[E(\omega)] = -\frac{V_{bi}}{qWKT}\omega\frac{d_c}{d_\omega}$$

T is the testing temperature; E_a is obtained from the slope of the Arrhenius plot, and v_0 is extracted from the y-axis intercept, $\ln(2\pi v_0)$.

Note S6. TPC and TPV

The m-TPV and TPC data were obtained through charge dynamics measurements. According to established methodologies, the parameters η_e and η_x are used as indicators of bulk defect concentration and interfacial transport capability, respectively. In this context, η_c is calculated as follows[18, 19]:

$$\eta_C(V) = 1 - \frac{\tau_{TPC}(V)}{\tau_{TPV}(V)}$$

where τ_{TPC} denotes the TPC decay time constant. The parameter η_{ext} derives from:

$$\eta_e(V) = \frac{IQE(V)}{\eta_C(V)}$$

with IQE(V) determined by:

$$IQE(V) = \frac{Q(V)}{Q(-1V)}$$

where Q(V) represents the integral charge obtained from the area under the TPC curve.

Note S7. Minority carrier diffusion length

The calculation formulas were as follows[11]:

$$IQE(\lambda,V) = \frac{EQE(\lambda,V)}{1 - R(\lambda)}$$

$$IQE(X_d,V) = \frac{exp(-\alpha(\lambda)X_d)}{1 + \alpha(\lambda)L_d}$$

$$L_d = \sqrt{\tau \mu_e k_B T/q}$$

where the EQE (λ, V), measured as a function of wavelength (λ) and voltage bias (V), obtained from EQE measurements, and R(λ) is determined from the reflectivity as a function of wavelength. The bias dependence of X_d is derived from the C–V measurement. The resulting IQE (X_d, λ) dataset is fitted to the analytic expression to extract a single L_d value, along with the absorption coefficient (α) at each λ.

References

1. Y. Wang, L. Wang, Y. Wang, X. Zhao, X. Zhang, X. Zhang and Y. Liu, *physica status solidi (RRL) – Rapid Research Letters*, 2023, **18**, 2300186.
2. M. Neuschitzer, K. Lienau, M. Guc, L. C. Barrio, S. Haass, J. M. Prieto, Y. Sanchez, M. Espindola-Rodriguez, Y. Romanyuk, A. Perez-Rodriguez, V. Izquierdo-Roca and E. Saucedo, *J. Phys. D: Appl. Phys.*, 2016, **49**, 125602.
3. L. Grenet, P. Grondin, K. Coumert, N. Karst, F. Emieux, F. Roux, R. Fillon, G. Altamura, H. Fournier, P. Faucherand and S. Perraud, *Thin Solid Films*, 2014, **564**, 375-378.
4. X. Li, Z. Su, S. Venkataraj, S. K. Batabyal and L. H. Wong, *Sol. Energy Mater. Sol. Cells*, 2016, **157**, 101-107.
5. B. Lin, Q. Sun, C. Zhang, H. Deng, Y. Li, W. Xie, Y. Li, Q. Zheng, J. Wu and S. Cheng, *ACS Appl. Energy Mater.*, 2023, **6**, 1037-1045.
6. X. Yang, B. Yao, Z. Ding, R. Deng, M. Zhao and Y. Li, *Micro Nanostruct.*, 2022, **163**, 107133.
7. H. Jeong, R. Nandi, J. Y. Cho, P. S. Pawar, H. S. Lee, K. E. Neerugatti, J. H. Kim and J. Heo, *Prog. Photovoltaics Res. Appl.*, 2021, **29**, 1057-1067.
8. K. S. Gour, P. S. Pawar, M. Lee, V. C. Karade, J. S. Yun, J. Heo, J. Park, J. H. Yun and J. H. Kim, *ACS Appl. Mater. Interfaces*, 2024, **16**, 30010-30019.
9. J. Lee, T. Enkhbat, G. Han, M. H. Sharif, E. Enkhbayar, H. Yoo, J. H. Kim, S. Kim and J. Kim, *Nano Energy*, 2020, **78**, 105206.
10. N. Ahmad, Y. Zhao, F. Ye, J. Zhao, S. Chen, Z. Zheng, P. Fan, C. Yan, Y. Li, Z. Su, X. Zhang and G. Liang, *Adv. Sci.*, 2023, **10**, 2302869.
11. Y. S. Lee, T. Gershon, O. Gunawan, T. K. Todorov, T. Gokmen, Y. Virgus and S. Guha, *Adv. Energy Mater.*, 2014, **5**, 1401372.
12. J. Wang, F. Meng, L. Lou, K. Yin, X. Xu, M. Jiao, B. Zhang, Y. Li, J. Shi, H. Wu, Y. Luo, D. Li and Q. Meng, *Nat. Energy*, 2026, **11**, 66-75.

13. M. Kamruzzaman, L. Chaoping, F. Yishu, A. K. M. Farid Ul Islam and J. A. Zapien, *RSC Adv.*, 2016, **6**, 99282-99290.
14. X. Pan, X. Li, Y. Yang, C. Xiang, A. Xu, H. Liu, W. Yan, W. Huang and H. Xin, *Adv. Energy Mater.*, 2023, **13**, 2301780.
15. Z. Su, G. Liang, P. Fan, J. Luo, Z. Zheng, Z. Xie, W. Wang, S. Chen, J. Hu, Y. Wei, C. Yan, J. Huang, X. Hao and F. Liu, *Adv. Mater.*, 2020, **32**, 2000121.
16. Y.-H. Zhao, Q.-Q. Gao, S.-J. Yuan, Q.-Q. Chang, T. Liang, Z.-H. Su, H.-L. Ma, S. Chen, G.-X. Liang, P. Fan, X.-H. Zhang and S.-X. Wu, *Chem. Eng. J.*, 2022, **436**, 135008.
17. H. S. Duan, W. Yang, B. Bob, C. J. Hsu, B. Lei and Y. Yang, *Adv. Funct. Mater.*, 2012, **23**, 1466-1471.
18. Y. Li, J. Shi, B. Yu, B. Duan, J. Wu, H. Li, D. Li, Y. Luo, H. Wu and Q. Meng, *Joule*, 2020, **4**, 472-489.
19. J. Zhou, X. Xu, H. Wu, J. Wang, L. Lou, K. Yin, Y. Gong, J. Shi, Y. Luo, D. Li, H. Xin and Q. Meng, *Nat. Energy*, 2023, **8**, 526-535.